Title
Operando Electrochemical Liquid-Cell 4D-STEM Studies of Dynamic Evolution of Cu Nanocatalysts for CO2 Reduction

Journal
Microscopy and Microanalysis, 29(Supplement_1)

ISSN
1431-9276

Authors
Yang, Yao
Shao, Yu-Tsun
Abruña, Héctor D
et al.

Publication Date
2023-07-22

DOI
10.1093/micmic/ozad067.665

Peer reviewed

Operando studies reveal active Cu nanograins for CO_2 electroreduction

Yao Yang[1,2,3†], Sheena Louisia[1,3†], Sunmoon Yu[3,4,†], Jianbo Jin[1], Inwhan Roh[1,3], Chubai Chen[1,3], Maria V. Fonseca Guzman[1,3], Julian Feijoo[1,3], Peng-Cheng Chen[1,5], Hongsen Wang[6], Christopher J. Pollock[7], Xin Huang[7], Yu-Tsun Shao[8], Cheng Wang[9], David A. Muller[8,10], Héctor D. Abruña[6,10] & Peidong Yang[1,3,4,5,*]

[1]Department of Chemistry, University of California, Berkeley, CA 94720, USA.
[2]Miller Institute for Basic Research in Science, University of California, Berkeley, CA 94720, USA.
[3]Chemical Sciences Division, Lawrence Berkeley National Laboratory, Berkeley, CA 94720, USA.
[4]Department of Materials Science and Engineering, University of California, Berkeley, CA 94720, USA.
[5]Kavli Energy NanoScience Institute, Berkeley, CA 94720, USA.
[6]Department of Chemistry and Chemical Biology, Cornell University, Ithaca, NY 14853, USA.
[7]Cornell High Energy Synchrotron Source, Cornell University, Ithaca, NY 14853, USA.
[8]School of Applied and Engineering Physics, Cornell University, Ithaca, NY 14853, USA.
[9]Advanced Light Source, Lawrence Berkeley National Laboratory, Berkeley, CA 94720, USA.
[10]Kavli Institute at Cornell for Nanoscale Science, Cornell University, Ithaca, NY 14853, USA.
*Corresponding author: p_yang@berkeley.edu

[†]Y.Y., S.L. and S.Y. contributed equally to this work.

Abstract:

CO_2 electroreduction facilitates the sustainable synthesis of fuels and chemicals[1]. Although Cu enables CO_2-to-multicarbon product (C_{2+}) conversion, the nature of the active sites under operating conditions remains elusive[2]. Importantly, identifying active sites of high-performance Cu nanocatalysts necessitates nanoscale, time-resolved *operando* techniques[3-5]. Here, we present a comprehensive investigation of the structural dynamics during the life cycle of Cu nanocatalysts. A 7 nm Cu nanoparticle ensemble evolves into metallic Cu nanograins during electrolysis, before completely oxidizing to single-crystal Cu_2O nanocubes upon post-electrolysis air exposure. *Operando* analytical and four-dimensional (4D) electrochemical liquid-cell scanning transmission electron microscopy (EC-STEM) reveals the presence of metallic Cu nanograins under CO_2 reduction conditions. Correlated high-energy-resolution time-resolved X-ray spectroscopy suggests that metallic Cu, rich in nanograin boundaries, supports undercoordinated active sites for C-C coupling. The quantitative structure-activity correlation shows a higher fraction of metallic Cu nanograins leads to higher C_{2+} selectivity. A 7 nm Cu nanoparticle ensemble, with a unity fraction of active Cu nanograins, exhibits 6 times higher C_{2+} selectivity than the 18 nm counterpart with one-third of active Cu nanograins. The correlation of multi-modal *operando* techniques serves as a powerful platform to advance our fundamental understanding of the complex structural evolution of nanocatalysts under electrochemical conditions.

Main text:

Copper remains the only heterogeneous electrocatalyst to selectively catalyze CO_2 reduction reaction (CO_2RR) to multicarbon (C_{2+}) products, including ethylene, ethanol, and propanol at appreciable rates[1,2]. Recent developments in *operando*/*in situ* methods, including advanced electron microscopy and synchrotron-based X-ray methods, provide powerful non-destructive tools to probe active sites and structural changes of electrocatalysts under reaction conditions[3-5]. However, there remains a lingering debate over the active state of Cu catalysts, regarding valence state or coordination environments under CO_2RR. For instance, some reports have proposed Cu^+ species and subsurface oxide as possible active sites of oxide-derived Cu electrocatalysts[6-9], while

others suggested the active state of bulk Cu catalysts is metallic[10-12] as subsurface oxides are not stable under negative potentials[13-15]. Another possible structural descriptor of locally enhanced CO_2RR activity has been reported to be micrometer-sized grain boundaries (GBs) on bulk metal electrodes[13-18]. Those studies probed the local activity at GBs with a μm-level spatial resolution, only suitable for bulk electrodes. Since C_{2+} product formation involves a C-C coupling step over multiple atomic Cu sites in close proximity[2], resolving catalytically active sites at or close to sub-nanometer resolution is necessary to uncover the structural origin of CO_2RR-active surfaces. In particular, *operando* methods with high spatiotemporal resolutions are instrumental in elucidating active sites of Cu nanoparticle (NP) electrocatalysts (<100 nm) among many other nanocatalysts[19].

This study presents a comprehensive structural picture of the life cycle for a family of high-performance Cu NP ensemble electrocatalysts, building upon our previous studies, which provided a baseline understanding of their structures[20-22]. An ensemble of monodisperse Cu NPs undergoes a structural transformation process (i.e., "electrochemical scrambling") where the surface oxide is reduced, followed by ligand desorption and formation of aggregated/disordered Cu structures that correlate with the formation of catalytically active sites for CO_2RR (Fig. 1a). The active Cu structures rapidly evolve into single-crystal Cu_2O nanocubes upon air exposure. Herein, we propose that active Cu nanograins play a critical role in the reduction/oxidation life cycle of these Cu nanocatalysts: (1) active sites for selectively reducing CO_2-to-C_{2+} products, and (2) highly reactive sites for breaking O=O bonds and inserting O atoms in the tetrahedral sites of Cu lattice.

A family of Cu NP (7, 10, and 18 nm) ensembles was studied to investigate the size dependence on their structural evolution dynamics. High-angle annular dark-field (HAADF) STEM images show the synthesized Cu NPs with narrow size distributions (Supplementary Fig. 1). Atomic-scale STEM image and corresponding electron energy loss spectroscopy (EELS) mapping of as-synthesized fresh 7 nm NPs exhibit a $Cu@Cu_2O$ core-shell structure with a metallic Cu core surrounded by ~2 nm oxide shell (Extended Data Figs. 1a,b and Supplementary Fig. 2). The 7 nm Cu NPs oxidized to Cu_2O NPs after air exposure for >5 h post-synthesis (Supplementary Figs. 3-4). We note that, whether 7 nm NPs are partially or fully oxidized, it does not impact the catalytic performance, since they likely reach a comparable active state during electrolysis (Supplementary Fig. 5). In contrast, both 10 and 18 nm NPs maintain a stable $Cu@Cu_2O$ core-shell structure over extended air exposure, suggesting that a minimum particle size of ~10 nm is required to form a self-passivated surface oxide layer (Extended Data Figs. 1c-f and Supplementary Figs. 6-10). This *ex situ* analysis of pristine Cu nanocatalysts provides necessary guidance for further *operando* electrochemical STEM (EC-STEM) studies (*vide infra*).

To track the dynamic morphological and structural evolution of Cu nanocatalysts and elucidate the nature of Cu active sites, we employed *operando* EC-STEM and four-dimensional (4D) STEM diffraction imaging. The *operando* EC-STEM cell encapsulates a liquid pocket with a three-electrode configuration, including Cu NPs deposited on the carbon working electrode, Pt counter and Pt pseudo-reference electrodes (WE, CE and RE)[23-25] (Fig. 1b). The redox potential and current density measured in the *operando* EC-STEM cell indicate the Cu NPs electrochemically behave consistently with standard H-cell measurements (Supplementary Figs. 11-13). A potential of -0.8 V versus reversible hydrogen electrode (RHE, all potentials are referenced to the RHE scale unless noted otherwise) was applied on the 7 nm NPs in the EC-STEM cell to simulate the optimal CO_2RR potential for C_{2+} product formation (Supplementary Fig. 14). The as-prepared EC-STEM cell has a liquid thickness of 500 nm or thicker[26], which is often too thick to resolve NPs <10 nm (Supplementary Fig. 15). Thus, we adopted a "thin liquid" strategy[27,28], performing a single linear

sweep voltammetry (LSV) scan from 0.4 to 0 V to trigger the hydrogen evolution reaction (typically co-existent during CO_2RR). The electrogenerated H_2 bubbles enable a thinner liquid film of ~100 nm, as quantified by liquid-cell EELS (Supplementary Fig. 16), leading to a significantly enhanced spatial resolution for tracking individual NPs in liquids (Supplementary Fig. 17 and Video 1). We observed that parts of the NP ensemble (lower part below the dashed line) already experienced noticeable particle aggregation right after the LSV scan (Fig. 1c). This points to the high reactivity/mobility of small Cu NPs even at potentials more positive than the onset of the CO_2RR (-0.4 V). *Operando* EC-STEM images captured at 0 V at an identical location show the dramatic aggregation of the remaining 7 nm NPs into Cu nanograins with sizes of 50-100 nm (Figs. 1d-e). Upon air exposure, small Cu nanograins (<50 nm) evolved into Cu_2O nanocubes while some large Cu nanoclusters (>100 nm) maintained an irregular morphology, possibly due to the loss of reactivity of bulk Cu with O_2[22]. Figures 1c-e serve as an overview of the electroreduction/oxidation life cycle of the 7 nm Cu NP ensemble.

To resolve the initial stage of the Cu nanograins formation, a mild potential of 0 V was applied on the 7 nm NP ensemble (Figs. 1f-i). *Operando* EC-STEM videos in this study were first recorded without applied potentials as control experiments to ensure no beam-induced damage occurred (Supplementary Video 2). After the initial LSV scan, Cu nanograins are observed and the remaining 7 nm Cu NPs experience rapid structural transformation, leading to the formation of new Cu nanograins and additional particle growth (Figs. 1f-h). A false-color STEM image of 0 and 24 s (red vs. green) illustrates the difference with the inset highlighting the particle growth process on existing Cu nanograins (Fig. 1i and Supplementary Fig. 18). At the C_{2+} optimal potential (-0.8 V), more dramatic particle movement occurred in the first 8 s, followed by progressive particle aggregation/coalescence (8-32 s) in Figs. 1j-m and Supplementary Video 3). Cu nanograins of 50-100 nm formed at -0.8 V approached a steady-state structure after an extended electroreduction for 90 s (Supplementary Fig. 19). Upon airflow, Cu nanograins rapidly evolved into ~100 nm well-defined Cu_2O nanocubes, similar to those formed after H-cell measurements (Supplementary Figs. 20, 21). In summary, *operando* EC-STEM of the 7 nm Cu NP ensemble identified two types of morphologies, loosely connected small Cu nanograins and closely packed large Cu nanograins, which may serve as active sites for CO_2RR.

Operando 4D-STEM diffraction imaging in liquid provides unique structural information beyond the traditional S/TEM imaging of morphological changes[27]. 4D-STEM uses a newly developed electron microscope pixel array detector (EMPAD), which can rapidly record a 2D electron diffraction pattern over a 2D grid of probe positions[29-32]. 4D-STEM with high sensitivity and dynamic range can significantly lower electron dose while retrieving nm-scale crystallographic information, which is indispensable for beam-sensitive materials in liquid. We focus on the structural transformation of the most active 7 nm NPs from the initial stage to the steady state of Cu nanograins followed by the post-electrolysis Cu_2O nanocubes formed upon air exposure (Fig. 2, left scheme). The HAADF-STEM image in Fig. 2a shows the 7 nm NP-derived loosely connected Cu nanograins formed at 0 V. A virtual bright-field (BF) STEM image, retrieved from 4D-STEM datasets, better reveals the fine granular features of Cu nanograins (Fig. 2b). One particular domain (Fig. 2c) was selected to show a diffraction pattern of a metallic Cu domain with Cu{111} (2.1 Å) and Cu{200} (1.8 Å) close to the Cu[110] zone axis. 4D-STEM dark-field imaging, based on diffraction spots of 1 (red), 2 (green) and 3 (blue), yielded a false-color map showing crystal domains with the same/similar crystal orientations resembling those three diffraction spots. 4D-STEM composite maps in Fig. 2d clearly show the highly polycrystalline

nature of active Cu with fine nanograins. Two particular regions highlight the nanograin boundaries which are either loosely connected (Fig. 2e) or closely overlapped (Fig. 2f). The Cu grains revealed in Figs. 2e-f are around 5-10 nm, which are comparable to that of pristine 7 nm Cu NPs. It indicates that pristine 7 nm Cu NPs serve as building blocks for forming nanograin boundaries, which are likely rich in defects and dislocations after the initial stage electroreduction at 0 V. Similar metallic Cu nanograins were widely observed in other 4D-STEM maps (Supplementary Fig. 22). To the best of our knowledge, this observation represents the first report of sub-10 nm nanograin boundaries supporting possible Cu active sites, at an unprecedented spatial resolution enabled by a probe size of ~1 nm.

After electroreduction at -0.8 V, the metallic Cu nanograins (50-100 nm) achieved a steady-state closely packed structure (Fig. 2g). A majority of diffraction patterns from Cu domains indicate polycrystalline metallic Cu (Fig. 2h). Few domains show a single-crystal-like metallic Cu feature close to the Cu[110] zone axis (Fig, 2i). It indicates that some Cu nanograins have sufficient driving force to reconstruct into highly crystalline Cu domains during the electroreduction at -0.8 V. False-color dark-field 4D-STEM maps, based on three diffraction spots in Fig. 2i, show that the majority of Cu nanograins are composed of individual grains separated by grain boundaries and/or stacking faults (white arrows, Fig. 2j). Interestingly, the Cu nanograins magnified in the dashed box in Fig. 2j show the predominant crystal orientation in green, resembling the diffraction spot 2 in Fig. 2i, and some metallic Cu nanograins on the surface with other crystal orientations in red, resembling the diffraction spot 1. This in-depth structural analysis indicates that the dominant active Cu sites, formed at -0.8 V, are closely packed and highly polycrystalline metallic Cu nanograins, relative to loosely connected Cu nanograins formed at 0 V.

Upon airflow to repel electrolyte, metallic Cu nanograins at the same location in the EC-STEM cell rapidly evolved into well-defined Cu_2O nanocubes (Fig. 2k). 4D-STEM diffraction patterns in Figs. 2l-n show that the Cu_2O nanocubes are single crystals with edge lengths of ~60-120 nm. We hypothesize that metallic Cu nanograins formed under bias are highly defective/disordered, which can be especially reactive to O_2 molecules. O=O bonds can dissociate and allow the spontaneous insertion of O atoms in the Cu lattice. In addition, *operando* EC-STEM of post-synthesis Cu_2O nanocubes under bias shows the fragmentation of large cubes (~100 nm) and redeposition of small nanoclusters (<20 nm), which is drastically different from the structure of metallic Cu nanograins (50-100 nm) formed at -0.8 V (Supplementary Fig. 23 and Video 4). This suggests that metallic Cu nanograins can only be derived from the 7 nm Cu NP ensemble and cannot be reversibly obtained from post-electrolysis Cu_2O nanocubes. As demonstrated by the loss of C_{2+} selectivity/activity upon utilizing these post-electrolysis nanocubes (Supplementary Fig. 24), only the metallic Cu nanograins obtained through the assembly and reconstruction of self-assembled Cu NPs can serve as the supporting structure for CO_2RR-active undercoordinated Cu sites. In summary, *operando* EC-STEM suggests the 7 nm Cu NP ensemble evolves into polycrystalline/disordered Cu nanograins, and transforms into single-crystal Cu_2O nanocubes post-electrolysis.

Similar to 7 nm NPs, 10 nm NPs experienced substantial particle movement/aggregation during the first 8 s at -0.8 V and continued to grow into larger Cu nanograins (50-100 nm) (Fig. 3a-d, Supplementary Figs. 25-26 and Video 5). Meanwhile, the 18 nm Cu NP ensemble displayed a distinctly different structural evolution. After an initial LSV to 0 V, 18 nm Cu NPs on the carbon WE partially aggregated and formed intriguing "melting" features at the initial stage (Figs. 3e-f). Subsequent air exposure led to the transformation of the metallic nanograins into well-defined

Cu_2O nanocubes while the nearby unreacted 18 nm Cu NPs remained unchanged (Fig. 3g, Supplementary Fig. 27). At -0.8 V, 18 nm Cu NPs experienced progressive particle reconstruction and migration (Figs. 3i-k) and agglomerated into large Cu nanograins over ~4 min (Supplementary Fig. 28 and Video 6). The limited and slower structural reconstruction of the larger NPs likely originates form their intrinsically lower surface energy. Additionally, larger NPs are packed less closely due to restricted interdigitation of their surface ligands in comparison to the smaller NP ensemble[33,34]. As a result, the initial aggregation of 10 and 18 nm Cu NPs is less dramatic than the 7 nm Cu NPs, leading to a lower density of nanograin boundaries and less active undercoordinated Cu sites. This hypothesis is corroborated by Pb underpotential deposition (UPD) that indicates a higher density of undercoordination sites on the 7 nm Cu NP ensemble (Supplementary Fig. 29).

The particle aggregation dynamics of 18 nm Cu NPs are illustrated in the structural model in Fig. 3h. We posit that the surface oxide of 18 nm Cu NPs is reduced and the NPs form metallic Cu nanograins with surface-active sites ($Cu@Cu^s$) in a more closely packed structure. This hypothesis was supported by *operando* resonant soft X-ray scattering (RSoXS)[34] using the same liquid-cell setup as *operando* EC-STEM (Fig. 3l). At 0 V, the X-ray scattering intensity of Cu increased dramatically, relative to the pristine 18 nm Cu NP ensembles. This indicates a higher level of aggregation of Cu NPs per unit area, leading to stronger X-ray scattering, which is consistent with the formation of denser "melting" feature in EC-STEM (Fig. 3f). At -0.8 V, the X-ray intensity remained at a similar level but exhibited a noticeable shift of the first minimum to a higher Q value, which corresponds to an average grain size smaller than pristine 18 nm Cu NPs by 2.9 ± 0.2 Å (one monolayer) (Supplementary Fig. 30). It suggests that although 18 nm Cu NPs, as building blocks, aggregated to form active Cu nanograins, only the surface 2 nm oxide layer participated in forming a lower density of nanograin boundaries, thus resulting in a smaller contribution of active undercoordinated Cu sites. *Operando* RSoXS provides a statistically robust analysis of aggregation dynamics of Cu NPs complementing the *operando* EC-STEM studies.

Operando high-energy resolution fluorescence detected (HERFD) X-ray absorption spectroscopy (XAS) was then used to elucidate the valence state and coordination environment of the Cu NP ensemble under CO_2RR conditions and upon air exposure (Fig. 4). The electrochemical behavior of the Cu nanocatalysts was comparable in both the customized X-ray cell and H-cell without observation of beam damage on the Cu NPs in electrolyte (Supplementary Figs. 31-33). HERFD XAS enables a significantly higher energy resolution (~1 eV) than conventional solid-state fluorescence detector (50-200 eV),[10-12,35,36] enabling the detection of fine features in XANES pre-edge regions (Supplementary Figs. 34-36). HERFD XANES of the 7 nm Cu NP ensemble revealed the same pre-edge energy as bulk Cu_2O (Fig. 4a), supporting the NPs are fully oxidized after being stored in air as previously shown by EELS (Supplementary Fig. 3). The chemical state of the Cu NPs was then investigated under CO_2RR. At -0.8 V, the NP ensemble displayed similar edge features to Cu foil. The observed transition to metallic Cu is consistent with the formation of the Cu nanograins observed with 4D-STEM (Fig. 2). Upon post-electrolysis air exposure, the NPs completely re-oxidize to Cu_2O. The high energy resolution of HERFD XANES enabled us to carry out an accurate quantitative analysis of the valence states achieved throughout the NPs life cycle (Supplementary Figs. 37-39). The oxide volume fractions of NP ensembles, determined by XAS, are consistent with the oxide shell thickness in EELS analysis (Supplementary Fig. 40). The quantitative valence analysis over the course of electrolysis revealed the metallic Cu fraction increases from 0 to 100% over 1 h (Fig. 4b and Supplementary Fig. 41), which was corroborated by second-level tracking of electroreduction/oxidation kinetics at a constant photon energy

(Supplementary Figs. 42-43). These measurements testify that the electroreduction of the 7 nm Cu NPs was completed within ~30 min at -0.8 V.

HERFD XANES of 18 nm Cu NPs indicated an average composition of ~70% metallic Cu in the core and ~30% Cu_2O in the shell. These larger NPs experienced a similar transition to metallic Cu under electroreduction though less dramatic relative to the smaller NPs (Fig. 4c and Supplementary Fig. 44). In addition, the pre-edge peak after post-electrolysis air exposure suggested that 18 nm Cu NPs evolved into a mixed Cu and Cu_2O phase, matching the partial formation of nanocubes from EC-STEM studies (Fig. 3g). Quantitative valence analysis suggested that the electroreduction of 18 nm Cu NPs was confined to the surface Cu_2O layer and took a shorter time (~10 min) than their 7 nm NP counterparts (~30 min) while the partial reoxidation of metallic Cu occurred progressively over 1 hour (Fig. 4d, Supplementary Fig. 45).

Given all three types of Cu NP ensembles (7, 10, and 18 nm) show the complete conversion from partially/fully oxidized pristine NPs to fully metallic Cu nanograins (Supplementary Figs. 37 and 45-46), the fraction of active Cu nanograins is defined as the relative fraction of the pristine Cu NP ensemble that can be converted to metallic Cu active sites under electrochemical potentials (Fig. 4f). This quantitative value was then correlated to the CO_2RR performance of the different Cu NP ensembles (Fig. 4f-g, Supplementary Tables 1-2). The resulting structure-activity correlation suggests that a higher fraction of active Cu nanograins leads to a higher C_{2+} selectivity. In particular, the 7 nm Cu NP ensemble with 100% Cu nanograins shows a C_{2+} selectivity six times as high as the 18 nm Cu NP ensemble with only 32% Cu nanograins at -0.8 V. The activity and stability of these nanograins was also tested in a gas-diffusion electrode where the 7 nm Cu NP ensemble displayed a higher C_{2+} faradaic efficiency of (~57%) at a much higher current density of 300 mA/cm^2, relative to H-cell (~44%) at 15 mA/cm^2 (Supplementary Table 3). This demonstrates the 7 nm Cu NP-derived nanograins can also perform under industrially relevant conditions.

Further EXAFS analysis of the Cu NP ensembles provides additional details on their active structure (Fig. 4e, Supplementary Figs. 47-50). The scattering amplitude of the Cu-Cu peak for the 7 nm Cu NPs after 1 h electroreduction was noticeably lower than that of a standard Cu foil in Fig. 4e. Specifically, EXAFS fitting of the nanocatalyst after 1 h CO_2RR yields an average nearest Cu-Cu coordination number (CN) of ~8, suggesting the presence of undercoordinated Cu sites (Supplementary Fig. 50). Eventually, after 4 hours of electroreduction, the Cu-Cu CN approached a steady-state value of 12 comparable to that of Cu foil. Such an increase likely results from the continuous aggregation/coalescence of smaller Cu nanograins into fully grown Cu nanograins (50-100 nm) with a negligible contribution from undercoordinated surface Cu sites[37] (Supplementary Fig. 47). We hypothesize that while surface and bulk Cu become spectroscopically indistinguishable, since EXAFS is more sensitive to bulk than surface, undercoordinated sites are still present within the steady-state structure of the Cu nanocatalysts. This is corroborated by Pb UPD measurements indicating the presence of stronger binding sites formed on the 7 nm Cu NP ensemble (Supplementary Fig. 29).

Although our EXAFS results suggest that the slow structural change in the NP ensemble would lead to a variation of the nanocatalyst catalytic activity, we note that only the signal obtained after 4 hours is associated with the catalyst steady-state structure. Such slow kinetics result from the *operando* X-ray cell configuration and are otherwise much faster in the H-cell as demonstrated by the CO_2RR activity stabilized within 20 min and maintained for 4 hours onward (Supplementary Fig. 51). We further narrow down the time frame when the Cu NP ensemble structural transformation leads to the formation of C-C coupling active sites with *operando* differential

electrochemical mass spectrometry (DEMS) measurements with high temporal resolution, enabled by a dual thin-layer flow cell[38]. Specifically, C_2H_4 production reaches a steady state within the first 2.5 seconds in a DEMS flow-cell configuration, which is sufficiently fast compared to the ~20 min necessary to reach the steady-state structure and C_2H_4 production in an H-cell (Supplementary Fig. 52). The early-stage C_{2+} production demonstrated by DEMS ties back with the formation of Cu nanograins observed within the first few seconds under applied potentials in the EC-STEM cell. Meanwhile, the steady-state structure identified by *operando* XAS can be correlated to the steady-state activity measured in the H-cell (Supplementary Fig. 51). Overall, we can chronologically establish a structure-activity correlation that supports the catalytic significance of undercoordinated sites supported on Cu nanograins relevant to C_{2+} production.

In summary, this correlated *operando* study offers a comprehensive picture on the electroreduction/reoxidation life cycle of Cu nanocatalysts. Metallic Cu nanograins, rich in grain boundaries, support a high density of active undercoordinated sites that enhances the C_{2+} selectivity of the 7 nm Cu NP ensemble. This study represents a milestone towards spatially resolving the complex nature of active Cu sites for CO_2RR. Further statistical analysis of grain boundary density[13,39], grain-grain distance[40], and relative grain orientations[24] will provide additional insights on what structural factors of Cu nanograins are beneficial to C_{2+} formation. Inspired by the active Cu nanograins formation via rapid NP evolution, various approaches can be devised to utilize such structural transformation to generate nanocatalysts with higher C_{2+} intrinsic activity. For instance, smaller nanoparticles, clusters, or molecular complexes can be employed as smaller building blocks to generate a higher density of nanograin boundaries supporting undercoordinated active Cu sites. As proof of concept, a smaller sized Cu NP ensemble (~5 nm) was synthesized and demonstrated a distinctly higher C_{2+} selectivity (55%) at a lower Cu mass loading, relative to the 7 nm counterpart (44%, see Supplementary Note, Figs. 53-57, Video 7 and Table 4). We anticipate that correlation of *operando* structural studies with electron and X-ray probes and additional molecular-level spectroscopical methods will be necessary to unravel what intermediates bind and undergo C-C coupling on the active sites supported on those nanograin boundaries. This study emphasizes the importance and prospects of employing correlative *operando* methods to contribute to the rational design of future nanoscale electrocatalysts.

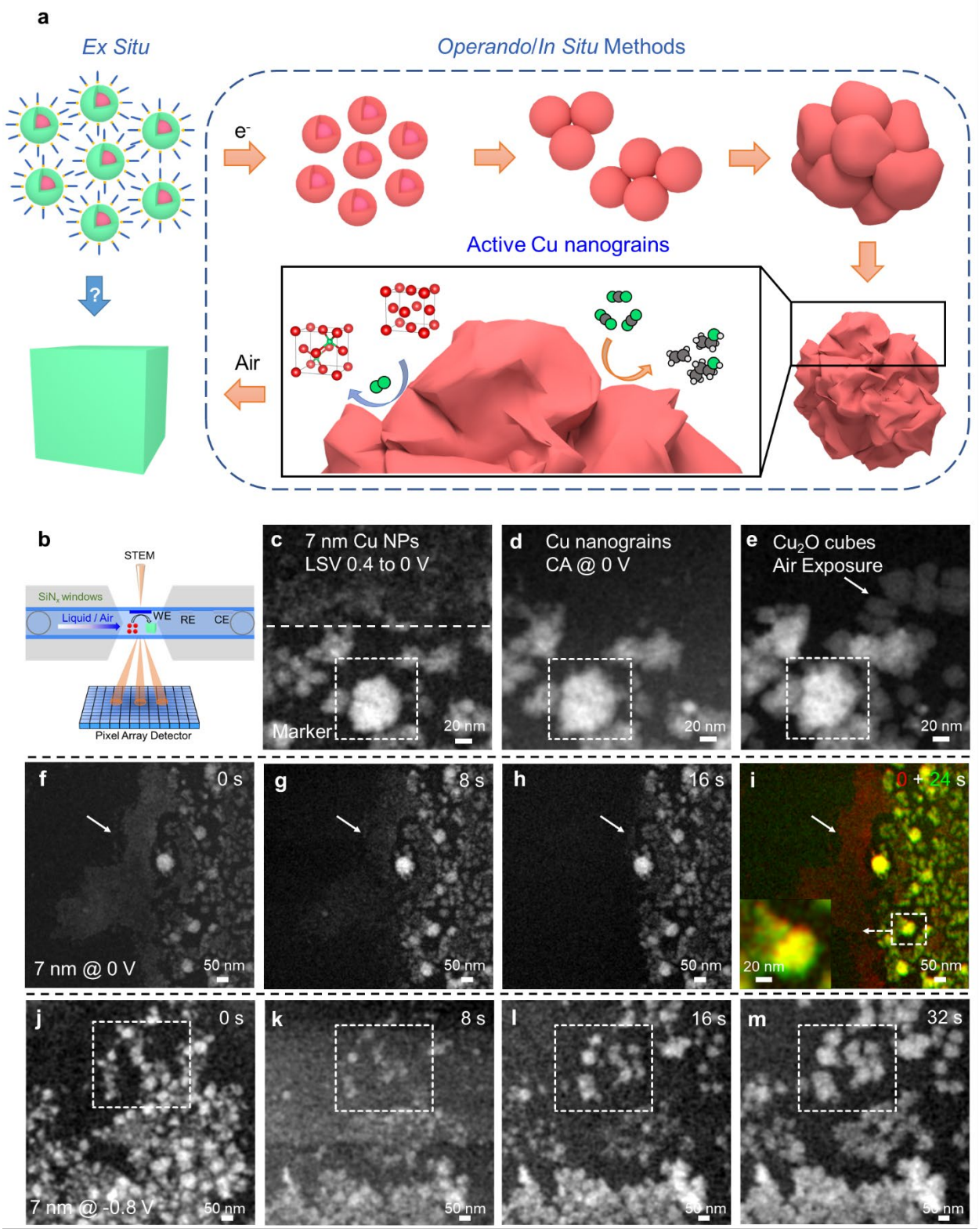

Figure 1. Scheme of the electroreduction/reoxidation life cycle of Cu nanocatalysts and *operando* EC-STEM studies of dynamic morphological changes of 7 nm nanocatalysts under various applied potentials. (a) Conventional *ex situ* methods are limited to the study of

nanocatalysts before/after CO_2RR. In contrast, *operando*/*in situ* methods used in this study, including EC-STEM and X-ray spectroscopy, uncover the dynamic changes in morphology, composition, and structure under real-time catalytically relevant conditions. An ensemble of monodisperse Cu NPs undergo a structural transformation during which the surface oxide is reduced, ligand are desorbed, and a progressive coalescence/aggregation leads to the formation of active metallic Cu nanograins. We propose those highly polycrystalline Cu nanograins are made of disordered grain boundaries that support undercoordinated Cu active sites for C_{2+} formation. Upon air exposure, Cu nanograins are also highly reactive for the O_2 bond breaking and insertion in the Cu lattice to form Cu_2O. **(b)** Schematic of *operando* EC-STEM and 4D-STEM with the capability to enable electrochemical measurements and simultaneously track morphological and structural changes under CO_2RR relevant conditions. (**c-e**) Overview of the life cycle of the 7 nm Cu nanocatalysts revealed by EC-STEM images of the initial growth after a single negative-going LSV scan from 0.4 to 0 V (**c**), further growth under CA at 0 V (**d**) and the post-electrolysis formation of Cu_2O cubes (marked by the arrow) upon air exposure at the identical location (**e**). (**f-i**) Morphological evolution of 7 nm NPs at 0 V vs. RHE. The false-color images in the inset of (**i**) highlight the newly formed regions in green after 24 s growth. (**j-m**) Further particle aggregation of 7 nm NPs at -0.8 V for 32 s with significant changes highlighted in the white box.

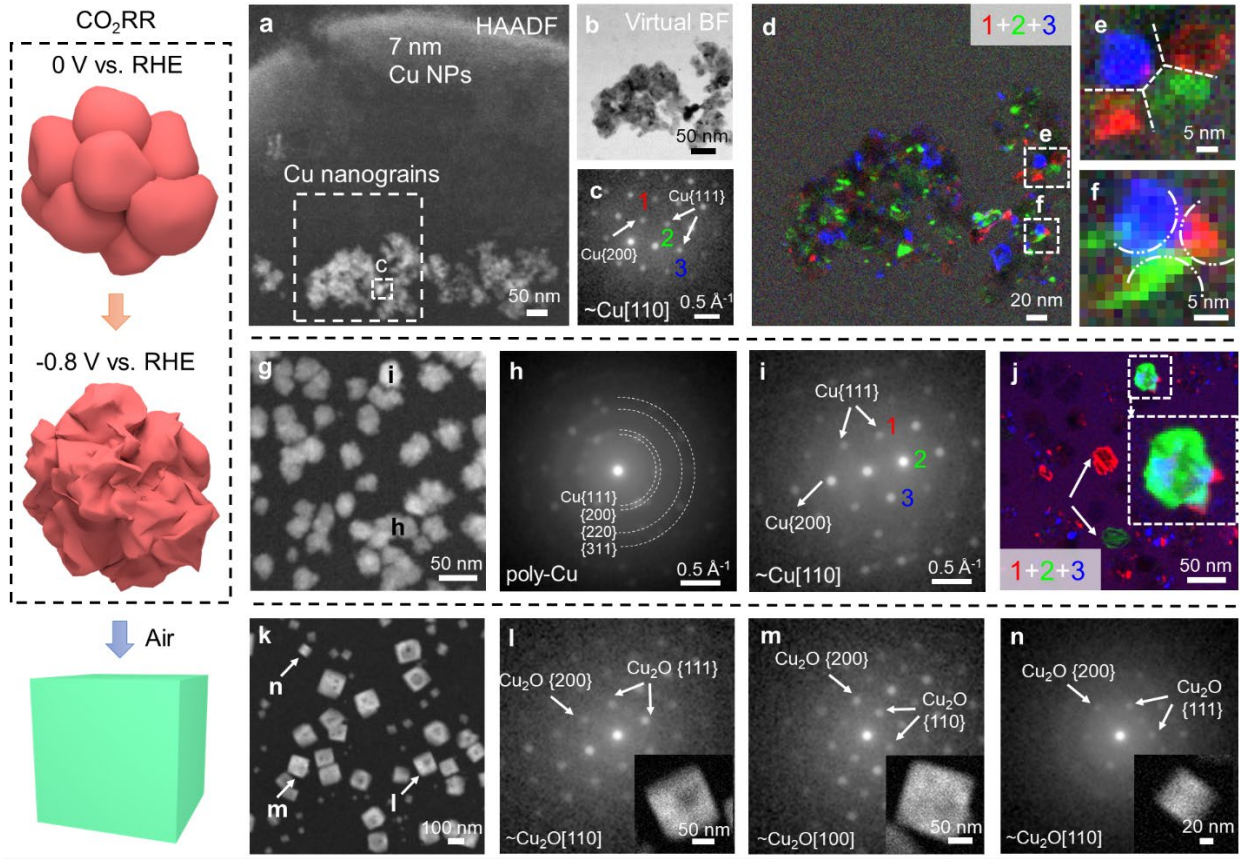

Figure 2. ***Operando*** **4D-STEM diffraction imaging of metallic Cu nanograins.** The left scheme serves as a visual guide of the structural evolution from initial stage of loosely connected (**a-e**) to steady-state closely packed (**g-i**) Cu nanograins followed by the formation of Cu_2O cubes (**k-n**) when exposed to air. (**a**) HAADF-STEM images of co-existing 7 nm NPs and loosely connected active Cu nanograins after the initial growth at 0 V. (**b**) Virtual bright-field (BF) STEM image of

Cu nanograins reconstructed from 4D-STEM datasets of the dashed box region in (**a**). (**c**) A representative electron diffraction pattern of one Cu domain in (**a**) showing the fcc metallic Cu with Cu{200} (1.8 Å) and Cu{111} (2.1 Å) close to [110] zone axis. (**d**) False-color dark-field 4D-STEM maps showing Cu nanograins with diffraction spots resembling those three marked as 1 (red), 2 (green) and 3 (blue), respectively, in (**b**). (**e**) Two particular regions, extracted from the dashed box in (**d**), showing the loosely connected Cu nanograins (**e**) and overlapping nanograin boundaries (**f**). (**g**) HAADF-STEM images of closely packed Cu nanograins formed at -0.8 V. (**h-i**) Representative diffraction patterns of highly polycrystalline Cu (**h**) and single-crystal-like Cu nanograins (**i**). (**j**) False-color dark-field 4D-STEM maps showing highly crystalline Cu nanograins with diffraction spots resembling those three marked as 1, 2, 3 in (**i**). (**k**) HAADF-STEM image of Cu_2O nanocubes formed upon air exposure. (**l-n**) Selective diffraction patterns of single-crystal Cu_2O cubes with d-spacings of {200} (2.1 Å), {111} (2.5 Å), or {110} (3.0 Å).

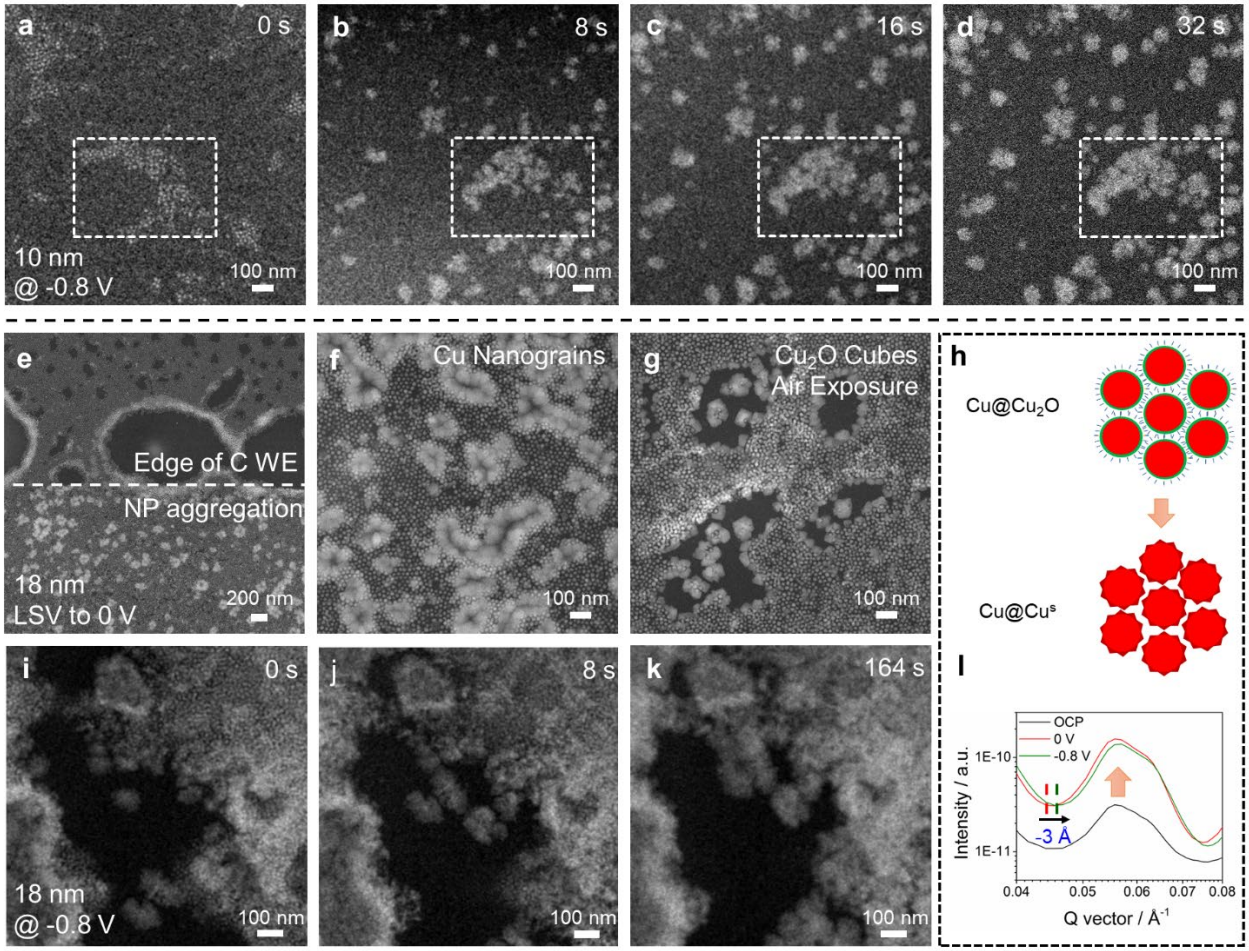

Figure 3. ***Operando*** **EC-STEM studies of dynamic morphological changes of 10 and 18 nm NPs.** (**a-d**) Selected *operando* EC-STEM video frames of the evolution of 10 nm NPs at -0.8 V. (**e-f**) EC-STEM image showing 18 nm NPs partially "melted" into Cu nanograins after initial growth after one LSV scan from 0.4 to 0 V. (**g**) STEM images of Cu_2O nanocubes formed from those Cu nanograins upon air exposure with nearby unreacted 18 nm NPs maintained the pristine morphology. (**i-k**) *Operando* EC-STEM images of the slower dynamic evolution of 18 nm NPs at -0.8 V for an extended time of 4 min, relative to 7 nm NPs. (**h, l**) Structural models showing the

transformation from 18 nm Cu NP ensembles to metallic Cu nanograins with surface Cu sites (Cu@Cu^s) and an average grain size smaller than pristine NPs by ~3 Å, which was supported by *operando* resonant soft X-ray scattering studies using the same liquid-cell TEM holder.

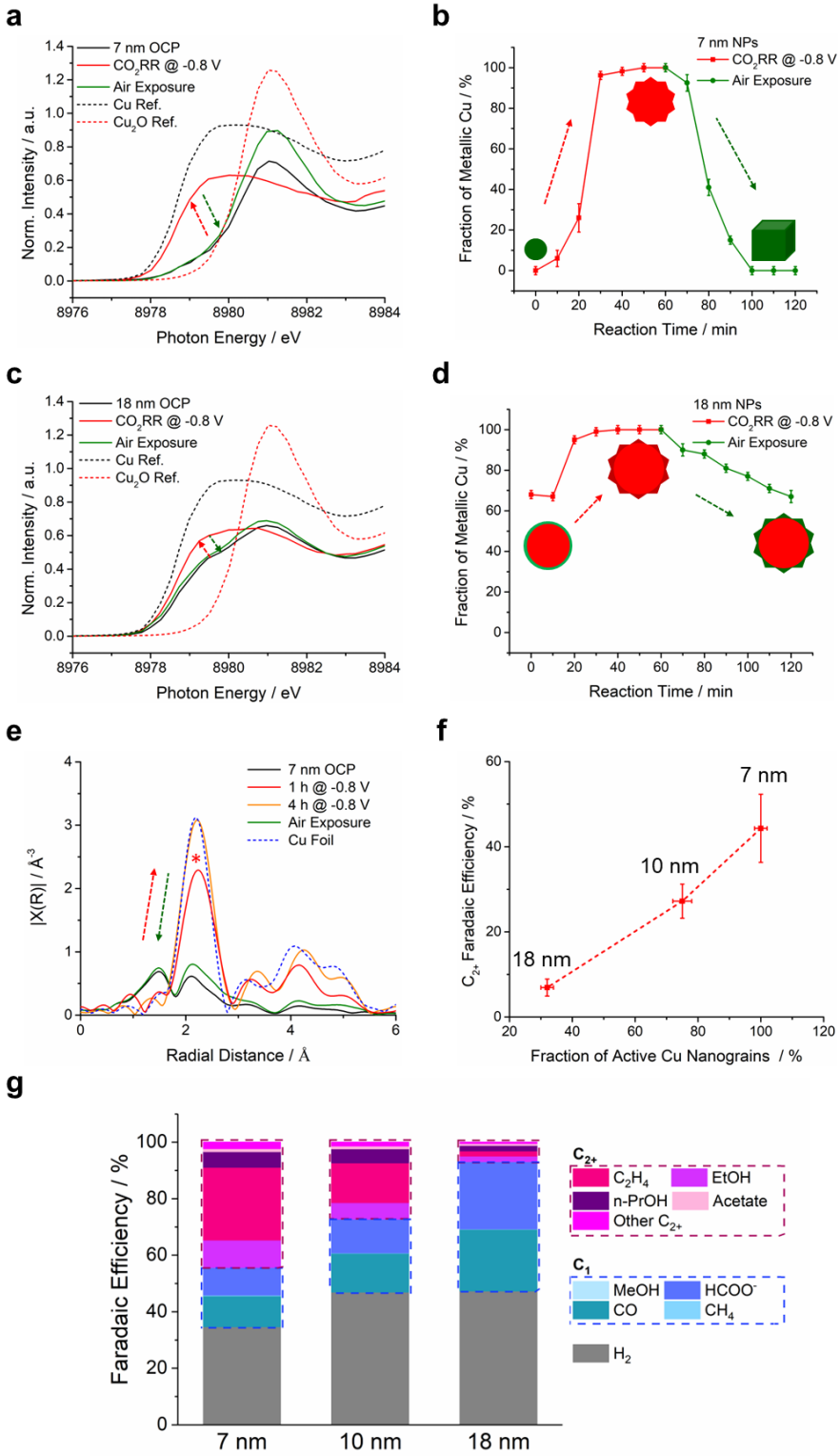

Figure 4. *Operando* HERFD XAS studies of the valence state and coordination environment of Cu nanocatalysts during their electroreduction/reoxidation life cycle. (**a**) *Operando* HERFD XANES spectra of pristine 7 nm NPs, metallic Cu formed at -0.8 V under CO_2RR conditions and Cu_2O cubes formed upon post-electrolysis air exposure, along with the standard references of bulk Cu and Cu_2O in dashed lines. (**b**) Quantitative analysis of relative fraction of metallic Cu showing the conversion from Cu_2O NPs to fully metallic Cu nanograins and the reoxidation of Cu nanograins to Cu_2O nanocubes upon air exposure. (**c-d**) *Operando* HERFD XANES and corresponding quantitative analysis of 18 nm NPs at -0.8 V showing the transformation from Cu@Cu_2O NPs to fully metallic Cu nanograins and the reoxidation of those Cu nanograins to mixed phases of Cu/Cu_2O upon air exposure. The electroreduction/reoxidation cycle was confined to the surface oxide layer. (**e**) *Operando* HERFD EXAFS of 7 nm under CO_2RR conditions and upon air exposure with EXAFS after 1 h electroreduction, suggesting the presence of undercoordinated Cu sites as highlighted by the red asterisk. (**f**) Structure-activity correlation of relative fraction of active Cu nanograins and C_{2+} faradaic efficiency of the Cu NP ensembles with three different NP sizes. (**g**) Faradaic efficiency for all CO_2RR products grouped as C_{2+}, C_1 products, and H_2 obtained from ensembles of three different Cu NP sizes at -0.8 V in an H-cell.

References

1. Ross, M. B. *et al*. Designing materials for electrochemical carbon dioxide recycling. *Nat. Catal*. **2**, 648-658 (2019).
2. Birdja, Y. Y. *et al.* Advances and challenges in understanding the electrocatalytic conversion of carbon dioxide to fuels. *Nat. Energy* **4**, 732-745 (2017).
3. Yang, Y. et al. *Operando* Methods in Electrocatalysis. *ACS Catal*. **11**, 1136-1178 (2021).
4. Mefford, J. T. *et al*. Correlative operando microscopy of oxygen evolution electrocatalysts. *Nature* **593**, 67-73 (2021).
5. Vavra, J., Shen, T. H., Stoian, D., Tileli, V. & Buonsanti, R. Real-time monitoring reveals dissolution/redeposition mechanism in copper nanocatalysts during the initial stages of the CO_2 reduction reaction. *Angew. Chem. Int. Ed*. **60**, 1347-1354 (2021).
6. Hahn, C. et al. Engineering Cu surfaces for the electrocatalytic conversion of CO_2: Controlling selectivity toward oxygenates and hydrocarbons. *Proc. Natl. Acad. Sci. USA* **114**, 5918-5923 (2017).
7. Li, C. W., Ciston, J. & Kanan, M. W. Electroreduction of carbon monoxide to liquid fuel on oxide-derived nanocrystalline copper. *Nature* **508**, 504-507 (2014).
8. Arán-Ais, R. M., Scholten, F., Kunze, S., Rizo, R. & Roldan Cuenya, B. The role of in situ generated morphological motifs and Cu(i) species in C_{2+} product selectivity during CO_2 pulsed electroreduction. *Nat. Energy* **5**, 317-325 (2020).
9. Eilert, A. *et al*. Subsurface oxygen in oxide-derived copper electrocatalysts for carbon dioxide reduction. *J. Phys. Chem. Lett*. **8**, 285-290 (2017).
10. Chang, C.-J. *et al.* Dynamic reoxidation/reduction-driven atomic interdiffusion for highly selective CO_2 reduction toward methane. *J. Am. Chem. Soc* **142**, 12119-12132 (2020).
11. Kimura, K, W. *et al.* Selective electrochemical CO_2 reduction during pulsed potential stems from dynamic interface. *ACS Catal*. **10**, 8632-8639 (2020).
12. Li, J. et al. Copper adparticle enabled selective electrosynthesis of n-propanol. *Nat. Commun*. **9**, 4614 (2018).
13. Lum, Y. & Ager, J. W. Stability of Residual Oxides in Oxide-Derived Copper Catalysts for

Electrochemical CO_2 Reduction Investigated with ^{18}O Labeling. *Angew. Chem. Int. Ed.* **57**, 551–554 (2018).
14. Fields, M., Hong, X., Nørskov, J. K., Chan, K. Role of subsurface oxygen on Cu surfaces for CO_2 electrochemical reduction. *J. Phys. Chem. C* **122**, 16209-16215 (2018).
15. Garza, A. J., Bell, A. T. & Head-Gordon, M. Is Subsurface Oxygen Necessary for the Electrochemical Reduction of CO_2 on Copper? *J. Phys. Chem. Lett* **9**, 49 (2018).
16. Feng, X., Jiang, K., Fan, S. & Kanan, M. W. A Direct Grain-Boundary-Activity Correlation for CO Electroreduction on Cu Nanoparticles. *ACS Cent. Sci*. **2**, 169-174 (2016).
17. Mariano, R. G., McKelvey, K., White, H. S. & Kanan, M. W. Selective increase in CO_2 electroreduction activity at grain-boundary surface terminations. *Science* **358**, 1187-1192 (2017).
18. Mariano, R. G. *et al.* Microstructural origin of locally enhanced CO_2 electroreduction activity on gold. *Nat. Mater.* **20**, 1000-1006 (2021).
19. Yang, Y. et al. Electrocatalysis in alkaline media and alkaline membrane-based energy technologies. *Chem. Rev*. **122**, 6117-6321 (2022).
20. Hung, L., Tsung, C.-K., Huang, W., Yang, P. Room-temperature formation of hollow Cu_2O nanoparticles. *Adv. Mater.* **22**, 1910-1914 (2010).
21. Kim, D., Kley, C. S., Li, Y. & Yang, P. Copper nanoparticle ensembles for selective electroreduction of CO_2 to C_2–C_3 products. *Proc. Natl. Acad. Sci. USA* **114**, 10560-10565 (2017).
22. Li, Y. *et al*. Electrochemically scrambled nanocrystals are catalytically active for CO_2-tomulticarbons. *Proc. Natl. Acad. Sci. USA* **117**, 9194-9201 (2020).
23. Holtz, M. E. *et al.* Nanoscale imaging of lithium ion distribution during in situ operation of battery electrode and electrolyte. *Nano Lett.* **14**, 1453-1459 (2014).
24. Yang, Y., Shao, Y.-T., Lu, X., Abruña, H. D. & Muller, D. A. Metal monolayers on command: underpotential deposition at nanocrystal surfaces: a quantitative *operando* electrochemical transmission electron microscopy study. *ACS Energy Lett*. **7**, 1292-1297 (2022).
25. Williamson, M., Tromp, R. Vereecken, P., Hull, R. & Ross, F. Dynamic microscopy of nanoscale cluster growth at the solid–liquid interface. *Nat. Mater*. **2**, 532-536 (2003).
26. Holtz, M. E., Yu, Y., Gao, J., Abruña, H. D. & Muller, D. A. *In Situ* electron energy-loss spectroscopy in liquids. *Microsc. Microanal*. **19**, 1027-1035 (2013).
27. Yang, Y., Shao, Y.-T., Lu, X., Abruña, H. D. & Muller, D. A. Elucidating Cathodic Corrosion Mechanisms with *Operando* Electrochemical Transmission Electron Microscopy. *J. Am. Chem. Soc.* **144**, 15698-15708 (2022).
28. Serra-Maia, R. *et al.* Nanoscale chemical and structural Analysis during in situ scanning/transmission electron microscopy in liquids. *ACS Nano* **15**, 10228-10240 (2021).
29. Chen, Z. *et al*. Electron ptychorgraphy achieves atomic-resolution limits set by lattice vibrations. *Science* **372**, 826-831 (2021).
30. Tate, M. W. *et al*. High dynamic range pixel array detector for scanning transmission electron microscopy. *Microsc. Microanal*. **22**, 237-249 (2016).
31. Ophus, C. Four-dimensional scanning transmission electron microscopy (4D-STEM): From scanning nanodiffraction to ptychography and beyond. *Micro. Microanal*. **25**, 563-582 (2020).
32. Zuo, J. M. & Tao, J. Scanning Electron Nanodiffraction and Diffraction Imaging. In *Scanning Transmission Electron Microscopy*; Pennycook, S., Nellist, P., Eds.; Springer: New York, 2011.

33. Yu, S. *et al*. Nanoparticle assembly induced ligand interactions for enhanced electrocatalytic CO_2 conversion. *J. Am. Chem. Soc.* **143**, 19919-19927 (2021).
34. Yang, Y. *et al. Operando* resonant soft x-ray scattering studies of chemical environment and interparticle dynamics of Cu nanocatalysts for CO_2 electroreduction. *J. Am. Chem. Soc*. **144**, 8927-8931 (2022).
35. Glatzel, P. & Bergmann, U. High resolution 1s core hole X-ray spectroscopy in 3d transition metal complexes-electronic and structural information. *Coord. Chem. Rev*. 249, 65-95 (**2005**).
36. Yang, Y. *et al*. *In situ* X-ray absorption spectroscopy of a synergistic Co-Mn oxide catalyst for the oxygen reduction reaction. *J. Am. Chem. Soc.* **141**, 1463-1466 (2019).
37. Reske, R., Mistry, H., Behafarid, F., Roldan Cuenya, B. & Strasser, P. Particle size effects in the catalytic electroreduction of CO_2 on Cu nanoparticles. *J. Am. Chem. Soc.* **136**, 6978-6986 (2018).
38. Zeng, R. *et al.* Methanol oxidation using ternary ordered intermetallic electrocatalysts: A DEMS study. *ACS Catal*. **10**, 770-776 (2020).
39. Cao, L. et al. Mechanistic Insights for Low-overpotential electroreduction of CO_2 to CO on Copper Nanowires. *ACS Catal.* **7**, 8578-8587 (2017).
40. Jeong, H. M. *et al.* Atomic-scale spacing between copper facets for the electrochemical reduction of carbon dioxide. *Adv. Energy Mater.* **10**, 1903423 (2020).

Methods

Synthesis. 7 nm copper nanoparticles (NPs) were synthesized as previously reported by our group.[21] For larger nanoparticles, size was controlled by tuning the mole ratio of tetradecylphosphonic acid (TDPA) to copper(I) acetate (CuAc) precursors, where higher ratios resulted in larger particles. Specifically, to synthesize 7, 10, and 18 nm NPs, ratios of 0.5, 0.7, and 1.2, respectively, were used while maintaining the absolute concentration of CuAc (1 mmol). Synthesis of the 5 nm Cu NPs was adapted from a previous hot-injection method.[41] Additional synthesis details can be found in Supplementary Information.

Electrochemical measurements in H-cell. One monolayer of densely packed 7 nm NPs was achieved with a mass loading of 68.9 μg deposited on 1 cm^2 carbon paper (Sigracet 29AA, Fuel Cell Store). The design of the H-cell used in this study was described in detail previously[21,42]. Electrochemical measurements were performed in 0.1 M $KHCO_3$ at a CO_2 flow rate of 20 mL/min using a Biologic potentiostat, with Cu NPs supported on carbon paper as the working electrode (WE), Ag/AgCl (3 M KCl) as the reference electrode (RE) and a Pt wire as the counter electrode (CE), which was separated from the WE by an anion exchange membrane (Selemion AMV). All Faradaic efficiencies (FEs) reported herein are normalized while total FEs before normalization are in the range between 90 to 100%. Pb UPD measurement was conducted in a solution of 0.1 M $NaClO_4$, 10 mM $HClO_4$, and 3 mM $Pb(II)(ClO_4)_2$.[43]

***Operando* EC-STEM and 4D-STEM measurements**. *Operando* EC-STEM imaging was performed in CO_2-sat. 0.1 M $KHCO_3$ with a regular liquid thickness (~500 nm) in a Tecnai F-20 STEM. A Protochips Poseidon liquid-cell holder and Gamry potentiostatic were used for electrochemical measurements in EC-STEM. *Operando* EC-STEM image was acquired at a speed of 4 s/frame (1024×1024 pixels with a dwell time of 3 μs/pixel) at a beam dose of ~50 e^-/nm^2 per frame (dose rate of ~12.5 e^-/nm^2s). The low dose is critical to ensure no beam-induced damage so as to reliably track electrochemical reactions. A beam dose control experiment was routinely performed before each dynamic videos to ensure no evidence of beam damage. 4D-STEM experiments were performed using an electron microscope pixel array detector (EMPAD), by

recording a 2D diffraction pattern at each probe position, resulting in 4D datasets. The 4D-STEM diffraction imaging was performed with a probe size of ~1.3 nm in the full-width at half-maximum and 256×256 pixels at a dose of ~2,000 e^-/nm^2 (dose rate of ~6 e^-/nm^2s). Additional details can be found in Supplementary Information.

***Ex situ* STEM-EELS measurements**. *Ex situ* atomic-scale HAADF-STEM imaging and EELS were performed in a fifth-order aberration-corrected STEM (Nion UltraSTEM) operated at 100 keV with a semi-convergence angle of 30 mrad. EELS spectrum images were acquired with a 0.25 eV/channel energy dispersion in a Gatan spectrometer with a size of 100~200 pixels and an acquisition time of 10-20 ms/pixel. The Cu and O elemental maps were extracted using Cu $L_{3,2}$ and O K edges from EELS spectrum images and processed using principal component analysis and the linear combination of power law (LCPL) to subtract the background in ImageJ software.

***Operando* HERFD XAS measurements.** Cu K-edge XANES and EXAFS were acquired in HERFD mode at the PIPOXS beamline of the Cornell High Energy Synchrotron Source (CHESS) under ring conditions of 100 mA at 6 GeV. The incident energy was selected using a cryogenically-cooled Si(311) monochromator and focused using a pair of Rh-coated mirrors. The HERFD XAS selects one particular fluorescence decay channel, the Cu $K\alpha_1$ emission line at 8048 eV[36,37], by Si{444} single crystals in Rowland geometry. The sample was placed at an angle of 45° relative to the incident beam and fluorescence was detected using a Pilatus 100K detector, enabling the isolation of a decay transition from a single orbital with a much longer core hole lifetime. Given the energy-time uncertainty principle, it enables a significantly enhanced energy resolution on the order of 1 eV, relative to the typical 50-200 eV of conventional solid-sate fluorescence detector. The design of customized X-ray cell can be found in our previous report[37]. Cu NP catalysts were deposited on carbon paper as the working electrode with the same Cu loading as H-cell measurements. The reference electrode (Ag/AgCl (sat. KCl)) was placed (via a salt bridge) at the bottom of the cell to minimize the iR drop during electrochemical testing. Additional details can be found in Supplementary Information.

***Operando* resonant soft X-ray scattering measurements.** Soft X-ray measurements were performed in the same type of liquid cell setup (Protochips Inc.) as the *operando* EC-STEM holder with a liquid thickness of ~1 μm. Soft X-ray data were collected at the Advanced Light Source (ALS) beamline 11.0.1.2 with a back-illuminated Princeton PI-MTE CCD cooled to -45 °C. Scattering patterns of 18 nm NPs were collected for 0.6 s to minimize soft X-ray beam damage. RSoXS data fitting was conducted using software package Scatter.[44]

***Operando* DEMS measurement**s. Electrochemical measurements were performed with an EG&G Model 173 potentiostat/galvanostat, an EG&G Model 175 universal programmer and a DEMS setup. A monolayer of 7 nm NPs on a glassy carbon electrode (diameter = 1.0 cm) served as the working electrode with a mass loading of 8.14 $\mu g/cm^2$. Two Pt wires were employed as dual counter electrodes to minimize iR-drop. A Ag/AgCl (sat. KCl) was used as the reference electrode. DEMS measurements were performed in a dual thin-layer flow cell at a flow rate of 10 μL/s. A detailed description of the DEMS setup can be found in our previous work[38].

Additional References

41. Mantella, V. *et al.* Polymer lamellae as reaction intermediates in the formation of copper nanospheres as Evidenced by in situ X-ray studies. *Angew. Int. Chem. Ed*. **59**, 11627-11633 (2020).

42. Kim, D. *et al*. Selective CO_2 electrocatalysis at the pseudocapacitive nanoparticle/ordered-ligand interlayer. *Nat. Energy* **5**, 1032-1042 (2020).
43. Sebastiánsebastián-Pascual, P. & Escudero-Escribano, M. Surface characterization of copper electrocatalysts by lead underpotential deposition. *J. Electroanal. Chem*. **896**, 115446 (2021).
44. Förster, S., Apostol, L. & Bras, W. Scatter: Software for the analysis of nano- and mesoscale small-angle scattering. *J. Appl. Crystallogr.* **43**, 639-646 (2010).

Data availability

All relevant data are available from the corresponding author on request.

Supplementary Information:

Supplementary Figures 1-57, Tables 1-4, and Videos 1-7

Acknowledgement:

This work was supported by Director, Office of Science, Office of Basic Energy Sciences, Chemical Sciences, Geosciences, & Biosciences Division, of the US Department of Energy under Contract DE-AC02- 05CH11231, FWP CH030201 (Catalysis Research Program). Work at Cornell University (especially *operando* EC-STEM) was supported by the Center for Alkaline-Based Energy Solutions (CABES), an Energy Frontier Research Center (EFRC) program supported by the U.S. Department of Energy, under grant DE-SC0019445. This work made use of TEM facilities at the CCMR which are supported through the National Science Foundation Materials Research Science and Engineering Center (NSF MRSEC) program (DMR-1719875). This work also used TEM facilities at the Molecular Foundry was supported by the Office of Science, Office of Basic Energy Sciences, of the U.S. Department of Energy under Contract No. DE-AC02-05CH11231. This work is based upon research conducted at the CHESS which is supported by the National Science Foundation under award DMR-1332208. We thank the TEM technical support of J. Grazul and M. Thomas at Cornell, and R. Dhall and K. Bustillo at NCEM. We thank H. Celik and UC Berkeley's NMR facility in the College of Chemistry (CoC-NMR) for spectroscopic assistance. Instruments in the CoC-NMR are supported in part by NIH S10OD024998. We thank the initial discussion on *in situ* TEM with Dr. Yifan Li. We thank the X-ray cell fabrication by R. Page and S. McFall at the machine shop of Cornell LASSP. Y.Y. acknowledges the support from the Miller Research Fellowship. S.Y. acknowledges support from Samsung Scholarship. J.J. and C.C. acknowledge the support from Suzhou Industrial Park Scholarship.

Author contributions

Y.Y., S.L. and S.Y. designed the project under the guidance of P.Y. and H.D.A. Y.Y. performed atomic-scale STEM-EELS and *operando* EC-STEM measurements. Y.Y. performed *operando* 4D-STEM with the help of Y.-T.S. under the guidance of D.A.M. S.L. and I.R. synthesized Cu nanocatalysts and performed CO_2RR performance measurements with the help of M.V.F.G. and J.F.. S.Y. performed XRD analysis and H-cell measurements. I.R. performed GDE measurements. Y.Y. performed *operando* HERFD XAS studies with the help of S.L., S.Y. and X.H. C.J.P. provided generous support for the *operando* HERFD setup. Y.Y. performed *operando* RSoXS studies under the guidance of C.W. with the help of J.J. and C.C. H.W. and Y.Y. performed *operando* DEMS measurements. J.J. and C.C. prepared the scheme. Y.Y. S.L. and S.Y. wrote the manuscript under the supervision of P.Y. All authors revised and approved the manuscript.

Competing interests:

The authors declare no competing financial interest.

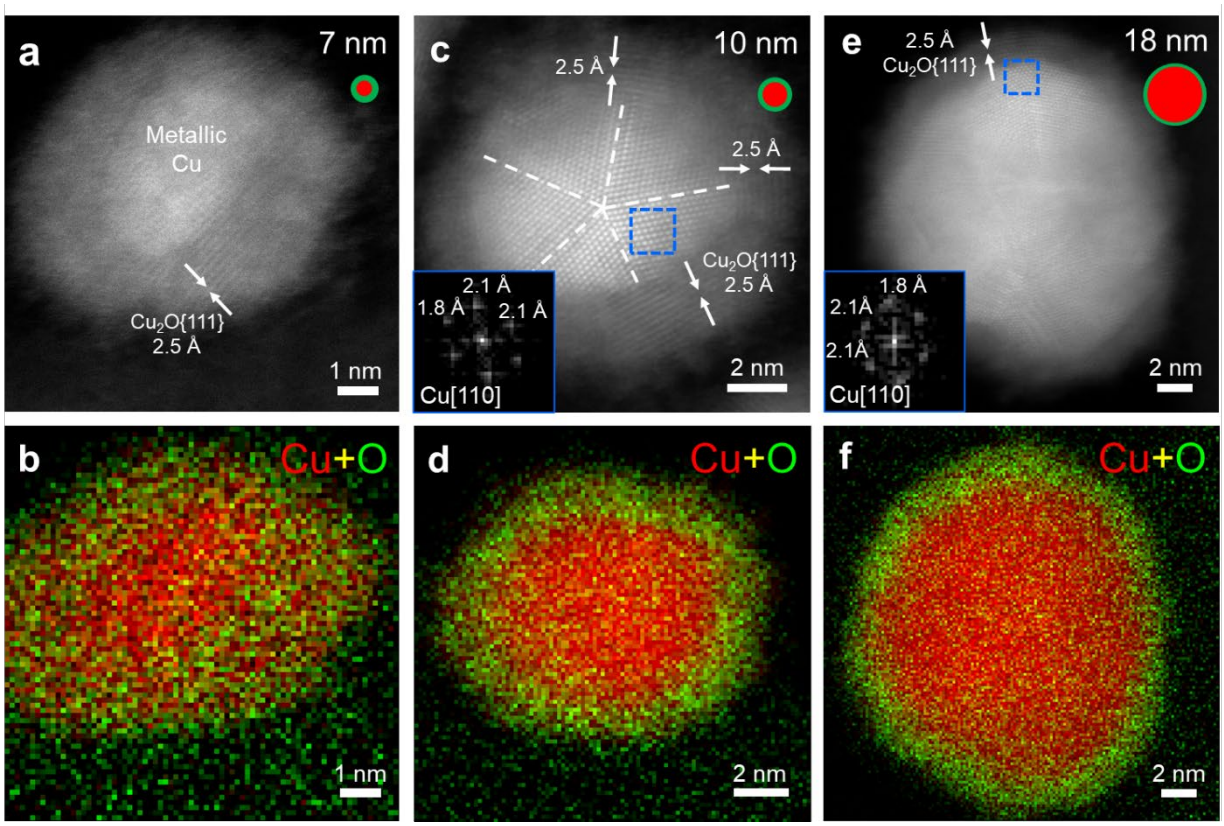

Extended Data Figure 1. Atomic-scale microstructures and chemical compositions of a family of Cu NP ensembles (7, 10, 18 nm). (**a-b**) HAADF-STEM image and EELS composite map of fresh 7 nm NPs with metallic Cu core (red) and ~2 nm oxide shell (green), which were oxidized to Cu_2O NPs after brief air exposure (Supplementary Fig. 3). (**c**) STEM image of 10 nm Cu@Cu_2O NPs with multi-domain Cu core close to the [110] zone axis surrounded by the Cu_2O shell with characteristic d-spacings of Cu_2O{111} (2.5 Å). (**d**) STEM-EELS composite map of 10 nm Cu@Cu_2O NPs with ~2 nm oxide shell. (**e-f**) STEM image of 18 nm Cu@Cu_2O NPs and EELS composite map showing the ~2 nm oxide shell.